



The Discrepancy between Observed and Predicted Heliospheric Energetic Neutral Atoms below Solar Wind Energy

André Galli¹ , Igor I. Baliukin² , Marc Kornbleuth³ , Merav Opher³ , Stephen A. Fuselier^{4,5} , Justyna M. Sokół⁴ ,
Konstantinos Dialynas⁶ , Maher A. Dayeh^{4,5} , Vladislav V. Izmodenov^{2,7} , and John D. Richardson⁸

¹ Physics Institute, University of Bern, Bern, Switzerland; andre.galli@unibe.ch

² Space Research Institute of Russian Academy of Sciences, Moscow, Russia

³ Boston University, Boston, USA

⁴ Southwest Research Institute, San Antonio, USA

⁵ University of Texas at San Antonio, San Antonio, USA

⁶ Center of Space Research and Technology, Academy of Athens, Athens, Greece

⁷ Lomonosov Moscow State University, Moscow Center for Fundamental and Applied Mathematics, Moscow, Russia

⁸ Massachusetts Institute of Technology, Cambridge, USA

Received 2023 June 23; revised 2023 July 25; accepted 2023 August 5; published 2023 September 1

Abstract

Measuring energetic neutral atoms (ENAs) allows for the remote observation of ion populations from the frontiers of our heliosphere. In this study, we compare the ENAs observed with the IBEX-Lo instrument onboard the Interstellar Boundary Explorer with ENA predictions from two heliosphere models. In contrast to previous studies, this paper presents model-data comparisons for the energy range 50 eV–2 keV over one full solar cycle not only in the upwind direction (Voyager 1 and Voyager 2 sky directions), but also for the north pole, south pole, port tail lobe, and downwind directions. The two heliosphere models produce the same basic result: there is a large gap (1 to 2 orders of magnitude in ENA intensity at 100 eV) between ENA data and model predictions between 100 and 500 eV for all sky directions. The reason for this gap is not understood yet. While some explanations are plausible and will be investigated in future studies, other explanations are excluded.

Unified Astronomy Thesaurus concepts: [Heliosphere \(711\)](#); [Interstellar medium \(847\)](#); [Space plasmas \(1544\)](#); [Heliosheath \(710\)](#)

1. Introduction

An energetic neutral atom (ENA) is formed when a fast ion (in this paper, usually a proton) exchanges its charge with an ambient neutral atom (in this paper, usually neutral hydrogen). The charge-exchange process includes a nearly negligible energy loss, so the ENA then leaves its place of origin with almost the same momentum as the parent ion on a ballistic trajectory and can reach an ENA instrument far away, for instance, the Interstellar Boundary Explorer (IBEX) at 1 au (McComas et al. 2009a), the Ion and Neutral Camera (INCA) on the Cassini spacecraft at ~10 au (Krimigis et al. 2009), or Neutral Particle Detector on Mars Express between the Earth and Mars orbit (Galli et al. 2013). The detected ENA intensity j_{ENA} is the line-of-sight integral from the instrument to infinity over the spatially varying proton intensity $j_p(r)$ multiplied by the spatially varying neutral hydrogen density $n_H(r)$ and the charge-exchange cross section $\sigma_{p,H}$:

$$j_{\text{ENA}} = \int_{\text{inst}}^{\infty} dr j_p(r) n_H(r) \sigma_{p,H}. \quad (1)$$

ENA imaging thus enables remote sensing of plasma regions. The interpretation of ENA measurements leads to an inversion problem because the measured ENA intensity represents a convolution of the local ion intensities (possibly belonging to different populations) and the local neutral densities. Models that combine ion populations with neutral densities are usually

required to identify and quantify the processes that gave rise to an observed ENA signal.

Generally, the observed ENAs are a sum of ENAs produced by various ion populations in the heliosheath and from the perturbed interstellar medium outside the heliopause. We use the term “heliosheath” to describe the region of the heliosphere between the solar wind termination shock and the heliopause. We presuppose that the plasma in the heliosheath consists of the thermal solar wind protons decelerated and heated up at the termination shock, pickup ions (PUIs) originating in the supersonic solar wind or at the termination shock, and of PUIs originating from neutral hydrogen in the heliosheath. A small fraction of the heliosheath was sampled in situ by Voyager 1 and Voyager 2 after their crossings from the termination shock at ~94 and ~84 au, respectively (e.g., Decker et al. 2005; Stone et al. 2005; Decker et al. 2008; Stone et al. 2008). After passing through the heliosheath, the Voyagers crossed the heliopause and entered the Very Local Interstellar Medium (VLISM) dominated by the perturbed interstellar medium (Zank 2015; Fraternali et al. 2020). Results from measurements and models from the dynamic heliospheric boundary regions can be found in Dialynas et al. (2022); Galli et al. (2022a); Kleimann et al. (2022); and references therein.

Early on in the IBEX mission, the observed heliospheric ENA emissions were separated into two categories: the IBEX Ribbon (McComas et al. 2009a) and the Globally Distributed ENA flux (GDF; Schwadron et al. 2011, 2014). This investigation concentrates on the latter ENA category. The IBEX Ribbon ENAs most likely originate outside the heliopause (McComas et al. 2009a, 2014; Swaczyna et al. 2016; Schwadron et al. 2018; McComas et al. 2020).

Secondary ENAs from PUIs (Chalov et al. 2010; Heerikhuisen et al. 2010; Zirnstein et al. 2016; Dayeh et al. 2019) are their most plausible source. The GDF, on the other hand, was traditionally assumed to originate predominantly from charge exchange between interstellar neutrals and plasma in the heliosheath (Fuselier et al. 2009a; McComas et al. 2009a; Hsieh et al. 2010; Schwadron et al. 2011; Galli et al. 2014).

The source processes for the GDF intensities measured below solar wind energies have remained under scrutiny; however, Zirnstein et al. (2018), for example, showed that solar wind protons and PUIs propagating down the heliotail and charge-exchanging with neutral hydrogen atoms as source terms could reproduce the observed GDF spectrum only if a strong stochastic acceleration of PUIs is assumed.

The complex ion energy spectrum inside the heliosheath (Dialynas et al. 2020), including the GDF ENA intensities, was used by Gkioulidou et al. (2022) showing an energy-dependent discrepancy between the model and the measurements over the energy range of 0.52–55 keV (also see discussion in Galli et al. 2022a; Kleimann et al. 2022; and references therein). Recently, Kornbleuth et al. (2023b) expanded on the basic model from Gkioulidou et al. (2022) by introducing a new population of PUIs accelerated via diffusive shock acceleration that become low-energy anomalous cosmic rays (ACRs), and thus eliminated the discrepancy between the modeled and observed GDF ENA fluxes over the ~ 0.5 –4 keV energy range. However, the discrepancy at ~ 4 to ~ 20 keV for the Belt ENAs (a broad region of enhanced ENA intensities centered at $\sim 260^\circ$ ecliptic longitude; Krimigis et al. 2009) is still persistent, suggesting the need for further acceleration of PUIs inside the heliosheath.

The most recent model-observation comparison at ENA energies below 1 keV (Fuselier et al. 2021; based on IBEX observations from 2009 to 2018) found that heliosheath PUIs can only account for 10% at most of the observed ENAs from the Voyager 2 direction. Hence, Fuselier et al. (2021) concluded that sources in the VLISM must be considered for these low energies, whereas the GDF at solar wind energies or above appears to have a much higher contribution (35%–100%) from ENAs created by charge exchange in the heliosheath. This is consistent with McComas et al. (2017) who used 7 yr of IBEX ENA observations to show that the GDF above 0.7 keV (the energy range covered by IBEX-Hi observations) and Ribbon evolve differently over time and therefore probably have different places of origin.

Our investigation revisits several possible sources of the GDF ENAs between 10 eV and 2 keV, presenting new results from two ENA models and discussing the discrepancy between these ENA model predictions and IBEX-Lo observations. The two ENA models are based on two independent heliospheric models developed by Izmodenov & Alexashov (2020) and by Kornbleuth et al. (2021a, 2023b). The two models rely on the same interstellar parameters and heliosphere boundary conditions, both modeling the cold solar wind plasma, hot PUIs, and electrons as one MHD fluid and calculating the neutral particle trajectories kinetically. The models differ in their treatment of PUIs and they use different algorithms to convert a given proton intensity into an ENA intensity.

2. ENA Observations

IBEX is a small explorer mission of NASA (McComas et al. 2009b) placed in an elliptical Earth orbit. IBEX carries two scientific instruments: the ENA imagers IBEX-Hi (Funsten

et al. 2009) and IBEX-Lo (Fuselier et al. 2009b). For this study, we concentrate on IBEX-Lo data. We rely on 11 yr average ENA intensities measured with IBEX-Lo (Tables 4 and 6 in Galli et al. 2022b); any IBEX-Hi data are taken from McComas et al. (2020). These data were corrected for the proper motion of the spacecraft and for ENA survival probabilities, and thus represent ENA intensities at 100 au in the solar inertial reference frame. Note, however, that the downwind and port tail lobe regions were sampled from IBEX-Lo anti-ram observations, leading to larger error bars (Galli et al. 2022b).

We only consider sky directions where contributions from Ribbon ENAs and interstellar neutrals (ISN) are negligible to focus on the GDF. The definitions of sky directions used in this study follow those by Galli et al. (2022b; see Figure 1).

For this comparison study, we select those results from the IBEX data that lend themselves most readily for comparison with models. We considered ENA energy spectra measured for Voyager 1 (246° – 270° ecliptic longitude, 30° – 54° latitude), Voyager 2 (282° – 306° ecliptic longitude, -42° to -18° latitude), north pole, south pole, port tail lobe, and downwind direction (see Figure 1). These are the most widely used test cases also by other model data comparisons (Fuselier et al. 2021; Gkioulidou et al. 2022; Kornbleuth et al. 2023b). The Ribbon pixel would be dominated by Ribbon ENAs at energies ≥ 200 eV, and ecliptic longitudes from 150° to 270° are dominated by the intense ISN signal at energies below 150 eV. For the spectra, only temporal averages over one full solar cycle are used. The energy range of the spectra represents the full range for which IBEX-Lo obtained reliable ENA intensities (50 eV–2 keV). IBEX-Hi data (0.7–6 keV) are also shown in the plots for reference.

All energy spectra from Galli et al. (2022b) used for this study are listed in Table 1. The tabulated energies differ for different directions because the applied Compton–Getting corrections depend on viewing direction. Below 50 eV, the ENA intensities derived from IBEX-Lo are challenging to constrain against the background sources (Fuselier et al. 2014; Galli et al. 2014), and the derived energy spectra entries below that energy are interpreted only as upper limits (Galli et al. 2022b). The ENA intensity reconstructed from the count rates in the lowest energy bin ($\simeq 15$ eV) is omitted from these tables and from all model comparisons because of the large uncertainties introduced by the Compton–Getting and survival probability correction in combination with possible local backgrounds at ENA energies below 50 eV.

3. Methodology

In this study, we compare the IBEX ENA data corrected for Compton–Getting and survival probabilities (Table 1) with the ENA intensities predicted with two different models. An alternative approach would be to propagate the ENA model predictions to expected count rates at the IBEX instruments. This approach would allow us to compare modeled versus measured full-sky ENA maps since the IBEX-Lo ENA maps at global central energy exist only in the spacecraft reference frame. This will be the subject of a future analysis. However, the corrections for survival probabilities and spacecraft motion introduce uncertainties in either approach.

3.1. ENA Sources

In the modeling, we consider three populations of ENAs that originate in the heliosheath: hydrogen ENAs are born in the

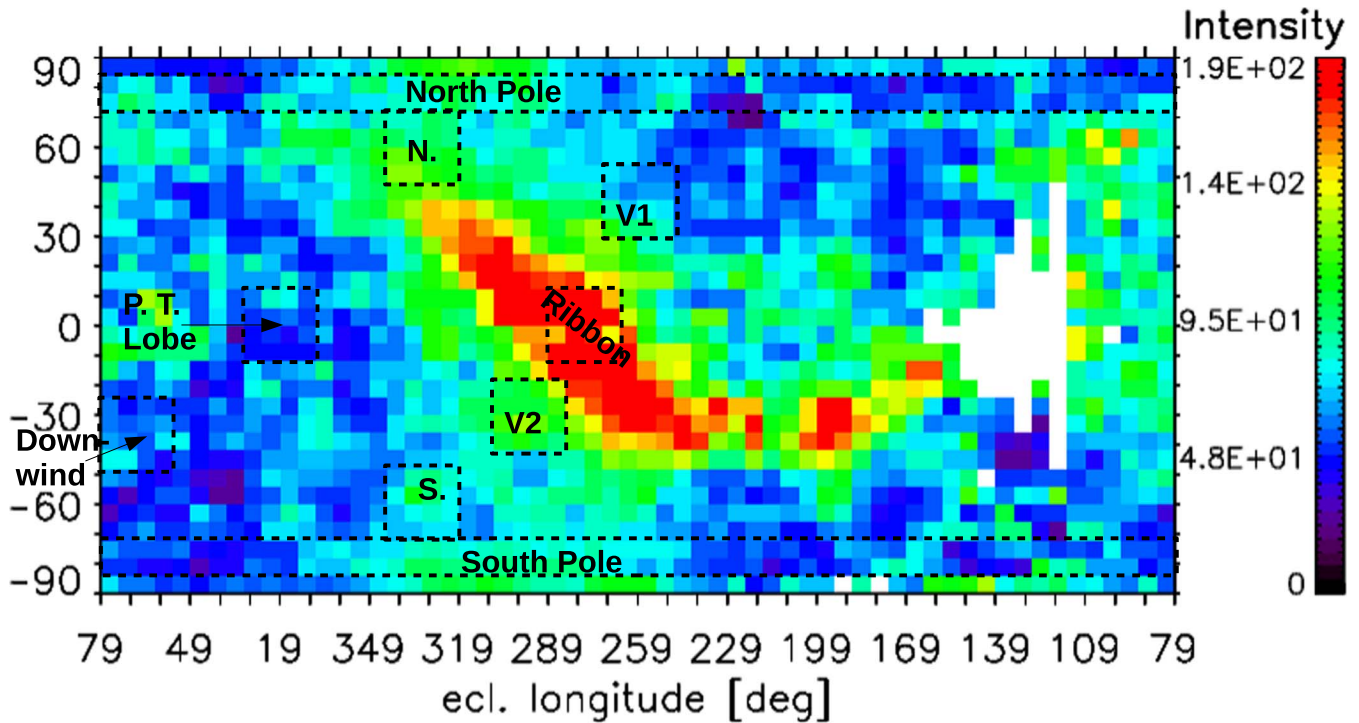


Figure 1. The sky regions defined by Galli et al. (2022b), plotted on an ENA intensity map of IBEX-Lo energy bin centered at 0.9 keV averaged over all 11 yr, including ComptonGetting and ENA survival probability correction. V1 and V2 denote Voyager 1 and Voyager 2 directions. Figure taken from Galli et al. (2022b).

charge exchange of (1) pickup protons created in the supersonic solar wind (SSW PUIs), (2) pickup protons created in the heliosheath (inner heliosheath (IHS) PUIs), or (3) thermal solar wind protons (SW protons). The first population of ENAs is the main contribution to the GDF at IBEX-Hi energies, while populations (2) and (3) are expected to provide signals at IBEX-Lo energy channels.

Besides ENAs, we consider primary ISN H that penetrates the heliosphere directly from the interstellar medium and secondary ISN H atoms from the VLISM (the so-called H-wall population). These populations of atoms produce fluxes at the two lowest energy channels of IBEX-Lo (see, e.g., Galli et al. 2019; Katushkina et al. 2021a, 2021b).

ENAs created in the VLISM are not included in our modeling. Previous works (e.g., Desai et al. 2014; Fuselier et al. 2021) have shown that such ENAs may play an important role in contributing to observed IBEX ENA fluxes. However, for the focus of this work, only ENAs created within the heliosheath, along with incident LISM and VLISM neutrals, are considered.

3.2. Models

To reproduce the observations made by IBEX-Lo, we use two global models of the heliosphere with different approaches to simulate the ENA fluxes, hereafter referred to as the Moscow and Boston models. The two models are characterized in more detail in the subsequent sections. Both global models are 3D kinetic-MHD models describing a single-ion plasma that combines the cold solar wind plasma, hot PUIs, and electrons as one fluid. The neutral particles are described kinetically using a Monte Carlo method. While two different ENA models are used in the different MHD models, Kornbleuth et al. (2021b, 2023b) showed that using the same ENA

model in both MHD solutions produced quantitatively similar ENA maps.

The interstellar parameters of the models are as follows: the proton and neutral H atom densities are $n_{p,ISM} = 0.04 \text{ cm}^{-3}$ and $n_{H,ISM} = 0.14 \text{ cm}^{-3}$, the bulk velocity and temperature are $V_{ISM} = 26.4 \text{ km s}^{-1}$ and $T_{ISM} = 6530 \text{ K}$, the direction of V_{ISM} is longitude = 75.4° , latitude = -5.2° in the ecliptic (J2000) coordinate system, the interstellar magnetic field intensity and orientation correspond to $B_{ISM} = 3.75 \text{ } \mu\text{G}$ and $\alpha = 60^\circ$, where the interstellar magnetic field vector lies in the hydrogen deflection plane (Lallement et al. 2005, 2010), and α is the angle between the interstellar bulk velocity and magnetic field vectors.

The two models use the same inner and outer boundary conditions, taken from Model 1 of Izmodenov & Alexashov (2020). For the inner boundary conditions, the models use the 22 yr averaged solar cycle conditions (1995–2017) as described in Appendix A of Izmodenov & Alexashov (2020), so the heliolatitudinal variations of the solar wind density and speed are considered. In the Moscow model, the inner boundary conditions are implemented at 1 au, while in the Boston model, they are set at 10 au by extracting the solar wind conditions from the Moscow model at that distance. At Earth, a Mach number $M = 6.44$ is used, corresponding to a solar wind temperature of $T_E = 188,500 \text{ K}$. For the solar magnetic field, the Parker spiral solution is assumed at 1 au with magnetic field magnitude $B_E = 37.5 \text{ } \mu\text{G}$ at 1 au.

3.3. The Moscow Model

The origin of this model can be traced back to the pioneering work of Baranov & Malama (1993), where they presented the first stationary axisymmetric self-consistent kinetic-gasdynamic model. Since then, the model has undergone significant advancements, incorporating various physical components

Table 1

Table of the ENA Energy Spectra Derived from IBEX-Lo Measurements Averaged over 11 yr, Corrected for Compton–Getting and Survival Probabilities (Galli et al. 2022b)

E	SP	E	NP	E	V1	E	V2	E	DW	E	Lobe
0.025	82640	0.025	86257	0.013	119018	0.012	52011	0.048	46639	0.057	65541
0.051	16752	0.051	11481	0.033	21970	0.031	12344	0.082	10396	0.091	12898
0.101	4879	0.101	4062	0.078	4666	0.074	5608	0.147	3616	0.159	5457
0.196	1319	0.196	1103	0.164	1372	0.159	1612	0.260	1133	0.275	1575
0.417	149	0.417	166	0.374	224	0.366	310	0.512	168	0.533	207
0.841	45	0.841	47	0.780	73	0.767	107	0.975	60	1.003	54
1.776	36	1.777	37	1.687	46	1.668	63	1.968	45	2.008	40

Note. Energies “E” are stated in units of keV, ENA intensities are given in units of $\text{cm}^{-2} \text{sr}^{-1} \text{s}^{-1} \text{keV}^{-1}$ for the sky regions “NP” = north pole, “SP” = south pole, “V1” = Voyager 1, “V2” = Voyager 2, “Lobe” = port tail lobe, and “DW” = downwind. The latter two directions were sampled from anti-ram observations. Uncertainties of ENA intensities: 30% for energies above 0.1 keV, 50% between 0.05 and 0.1 keV, and entries below 50 eV printed in red are upper limits.

such as galactic and anomalous cosmic rays (Myasnikov et al. 2000; Alexashov et al. 2004), interstellar helium ions, and SW alpha particles (Izmodenov et al. 2003), as well as interstellar oxygen and nitrogen (Izmodenov et al. 2004). In subsequent years, notable progress was made, with the model evolving into a time-dependent version (Izmodenov et al. 2005b) that integrated realistic SW data (Izmodenov et al. 2008). The stationary version of the model was expanded to three dimensions and the inclusion of the interstellar magnetic field was accounted for (Izmodenov et al. 2005a). Remarkably, this extended model demonstrated asymmetry in distances to the heliospheric termination shock, aligning well with Voyager 1 and Voyager 2 data (Izmodenov 2009).

Subsequently, Izmodenov & Alexashov (2015) enriched the 3D kinetic-MHD model by incorporating dynamic effects of the heliospheric magnetic field in the inner heliosheath and considering latitudinal variations of the SW parameters. Further improvements were made by Izmodenov & Alexashov (2020), where they identified a specific combination of magnitude and direction of the interstellar magnetic field ($B_{\text{ISM}} = 3.75 \mu\text{G}$, $\alpha = 60^\circ$) that yielded reasonably accurate positions of the heliopause along Voyager 1 and 2 trajectories during their actual crossings. The state-of-the-art version of the Moscow model includes the effect of thermal conduction, which reduces the thickness of the inner heliosheath and helps to reconcile the model results with Voyager observations (Izmodenov & Alexashov 2023).

In this paper, we employ plasma and neutral distributions obtained in the frame of the stationary simulations using Model 1 from Izmodenov & Alexashov (2020). The Moscow model has two unique features: (1) a rigorous kinetic treatment of the interstellar H atom component using a Monte Carlo method with splitting of the trajectories, and (2) a usage of Godunov-type numerical method with a specific, nonregular moving grid that allows for an exact fitting of the termination shock and the heliopause.

To obtain the ISN H distribution in the vicinity of the Sun precisely, the so-called local kinetic model is used, which takes into account non-Maxwellian kinetic features, radiation pressure, and ionization (for details see Katushkina & Izmodenov 2010; Katushkina et al. 2015). The local model of H distribution applies the boundary condition at the 70 au sphere from the simulations of the global model of the heliosphere by Izmodenov & Alexashov (2020). A sphere of 70 au is chosen as an outer boundary for the local model because it is entirely in the SSW and still far from the Sun, where the global Monte Carlo calculations are applicable. Inside the boundary sphere, the H distribution function is calculated by solving the kinetic

equation with the method of characteristics. The ISN H trajectories are modeled assuming the ratio $\mu = 1.258$ of the solar radiation pressure force to the solar gravitation force, as in Izmodenov & Alexashov (2015). This local model is used to simulate the fluxes of ISN H (primary and secondary) atoms observed by IBEX-Lo at 1 au.

The pickup proton distribution is calculated using the kinetic model by Baliukin et al. (2020). This model assumes the isotropic distribution of pickup protons in the solar wind rest frame and neglects velocity diffusion. The kinetic approach, among other things, allows for simulating the velocity distribution of the SSW PUIs and IHS PUIs separately and without any additional assumptions on the number densities and temperatures of these proton species. For the pickup proton distribution downstream of the termination shock, a bi-Maxwellian scenario is assumed (for details see Baliukin et al. 2022).

The velocity distribution of SW protons is assumed to be isotropic Maxwellian with the number density and temperature calculated based on the charged particles partitioning technique, which is described in detail in Section 4 of Baliukin et al. (2020). The pickup proton number density and pressure are calculated at a specific point in space and then subtracted from the total plasma number density and pressure known from the simulation of the global model, which uses a single-fluid approach for plasma. After accounting for the contribution of electrons and helium ions, the rest of the number density and pressure are attributed to the thermal SW protons. This technique needs an additional assumption about the electron temperature T_e . For this study, we assume $T_e = \beta T_{\text{sw}}$, where T_{sw} is the temperature of the SW protons, $\beta = 1$ in the region of the SSW, and $\beta = 6.7$ in the heliosheath (Chalov 2019).

In the Moscow model simulations, the observer (IBEX-Lo instrument) is placed at 1 au from the Sun in the ecliptic plane. Since IBEX-Lo observes ENAs in the plane perpendicular to the Sun-spacecraft vector, the ecliptic longitude of the spacecraft can be determined from the line of sight and type of observational geometry (either ram or anti-ram). Because Compton–Getting and survival probability corrections have been already applied to the IBEX-Lo data, we neglect the motion of the spacecraft (by setting its velocity to zero) and ionization losses of ENAs and ISN H atoms inside the termination shock in the modeling.

3.4. The Boston Model

The source of heritage of the Boston kinetic-MHD model (Kombreuth et al. 2021b) is the Outer Heliosphere model

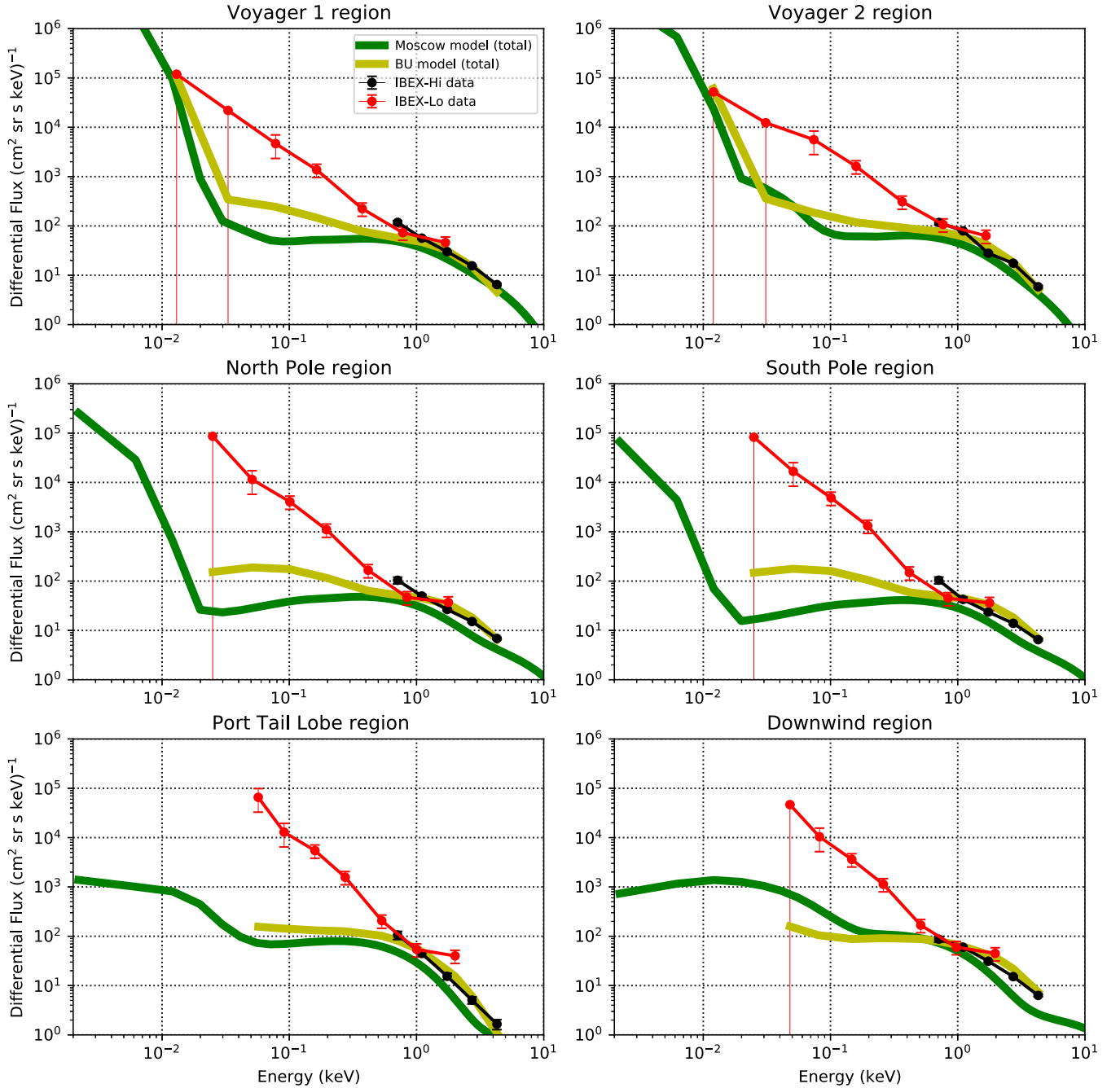


Figure 2. Measured vs. modeled total ENA intensities in the inertial reference frame at 100 au. IBEX observations are depicted by red (IBEX-Lo) and black circles (IBEX-Hi); the results of the Moscow model are shown in dark green and the results of the Boston model are shown in light green.

developed by Opher et al. (2003). It became a part of the BATS-R-US model (Powell et al. 1999) and later on a module of the Space Weather Modeling Framework (Tóth et al. 2005). The Boston model uses a single-fluid treatment of the plasma while modeling the neutrals kinetically using a direct simulation Monte Carlo method (Tenishev et al. 2021). Additionally, like the Moscow MHD model, the Boston University model assumes a unipolar solar magnetic field configuration in both hemispheres, as in Opher et al. (2015). This unipolar treatment eliminates spurious numerical effects due to numerical diffusion and reconnection of the solar magnetic field across the heliospheric current sheet (Michael et al. 2018).

The Boston ENA model is presented in Kornbleuth et al. (2021a, 2023b). This model assumes three subpopulations of

SSW PUIs at the termination shock (transmitted PUIs, reflected PUIs, and reflected PUIs further energized by diffusive shock acceleration at the termination shock) as well as the thermal SW ions. Beyond the termination shock, these ion populations do not undergo further acceleration in the heliosheath. The densities and energy fractions of each population relative to the plasma are obtained by fitting to hybrid simulations of ions across the termination shock by Giacalone et al. (2021). Details of the respective density and energy fractions of each population immediately downstream of the termination shock can be found in Table 1 of Kornbleuth et al. (2023b). The use of this model has greatly reduced the quantitative model-data discrepancies noted by Gkioulidou et al. (2022), who showed an energy-dependent discrepancy between ENA models and

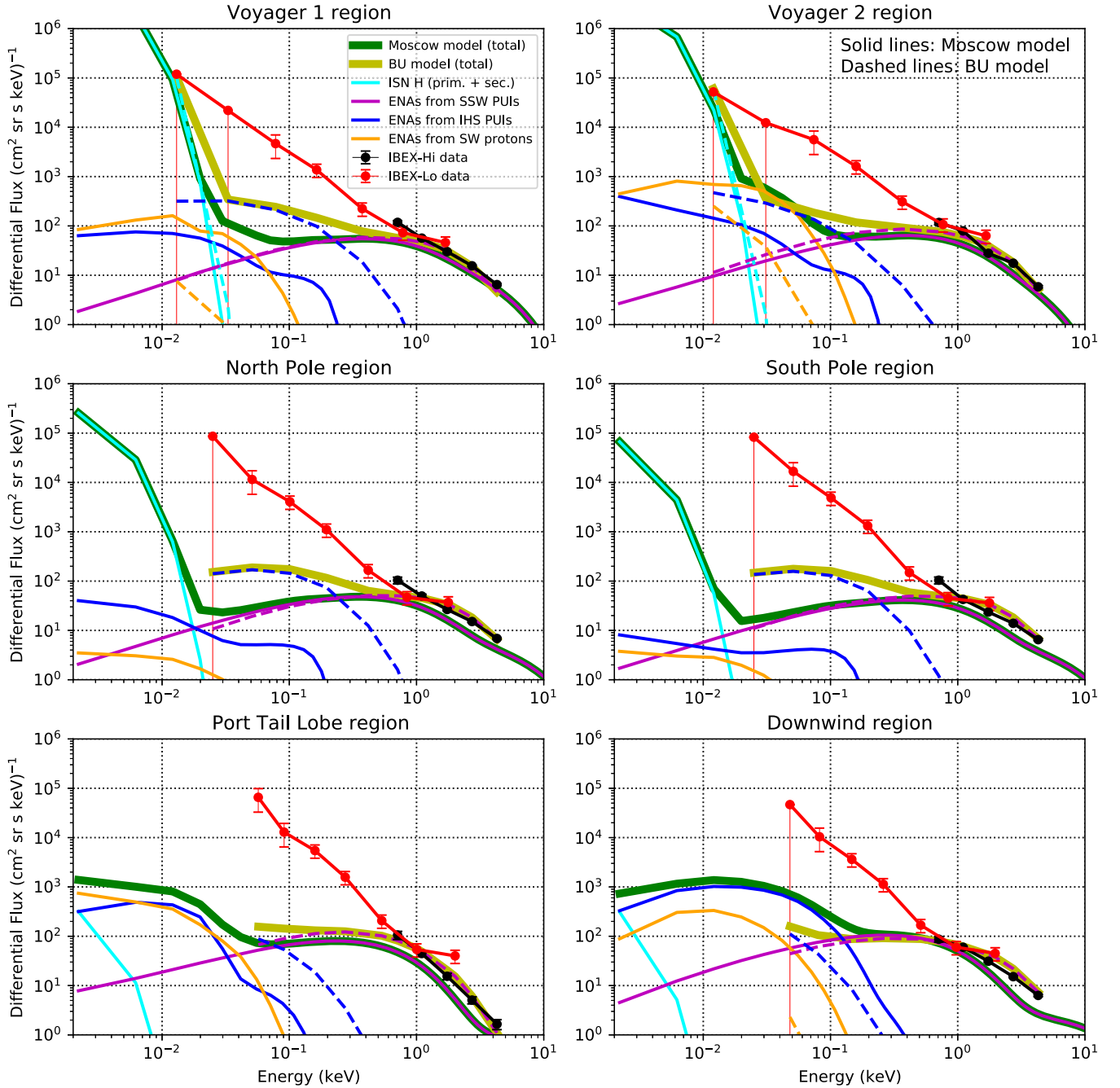


Figure 3. Measured vs. modeled total ENA intensities; the same as in Figure 2 but with contributions of the individual ENA populations. Cyan: ISN H contributions; purple: ENAs from solar wind PUI; blue: ENAs from heliosheath PUIs; orange: neutralized solar wind protons; the solid lines refer to the Moscow model populations and the dashed lines refer to Boston model populations.

observations, necessitating the inclusion of PUI acceleration in the heliosheath at high energies.

The Boston ENA model has been further updated from Kornbleuth et al. (2023b) in this work to compare the ENA predictions at IBEX-Lo energies. Whereas in Kornbleuth et al. (2023b) the incident flux from LISM and VLISM neutrals had been neglected, here the Boston model includes their contribution. Each population is modeled with a Maxwellian distribution with a single temperature as an approximation. These two sources correspond to the unperturbed interstellar medium and to the secondary ISN H (or hydrogen wall population). For ISN H trajectories, the model assumes an average $\mu = 1.0$. Additionally, photoionization of hydrogen

atoms is included for these populations assuming a photoionization rate of $8 \times 10^{-8} \text{ s}^{-1}$ at 1 au, which is an estimated solar minimum value (Bzowski et al. 2013).

PUIs created in the heliosheath had been previously ignored in the modeling of Kornbleuth et al. (2023b) due to their contributions at lower energies. Here, the IHS PUIs are included as well. As each of the three ion species (SW protons, SSW PUIs, and IHS PUIs) propagate from the termination shock along streamlines, they undergo charge exchange. The result of such a process is the creation of an ENA (which is potentially observable) and a low-energy ion likely with the characteristic properties of the LISM or VLISM neutrals. In the Boston ENA model, the newly created ion is assumed to be

picked up by the solar magnetic field in the heliosheath, with the pickup process yielding an IHS PUI temperature based on the relative velocities of the ion and the heliosheath plasma. Therefore, the IHS PUI temperature is given by

$$T_{p,IHS} = \frac{m_p}{2k_B}((u_{r,p} - u_{r,H})^2 + (u_{t,p} - u_{t,H})^2), \quad (2)$$

where m_p is the mass of the proton, k_B is the Boltzmann constant, $u_{r,i}$ is the radial component of the velocity for a given species, i , $u_{t,i}$ reflects the tangential (i.e., non-radial) components of the velocity for a given species, and the plasma and charge-exchanging neutral H species are denoted by p and H, respectively. The IHS PUIs are assumed to have Maxwellian distributions. No survival probability correction is applied to the modeled ENAs at heliocentric distances ≤ 100 au, as the observations already include this correction.

4. Results

The comparisons of IBEX observations (red circles: IBEX-Lo; black circles: IBEX-Hi) with ENA model predictions are shown in Figures 2 and 3 for all six sky regions for both the Moscow and the Boston model. The IBEX-Lo data correspond to Table 4 in Galli et al. (2022b). The difference between the two figures is that the former shows only the total ENA intensities from all model sources (dark green: Moscow model; light green: Boston model), whereas Figure 3 also shows the contributions from individual source populations of heliospheric ENAs and (lower energy) ISN H. ENA imagers only measure the sum of all neutral hydrogen atom populations. Thus, the data are to be compared with the thick green lines in Figures 2 and 3.

These figures show a substantial and significant (the uncertainties of data points are 1σ confidence intervals) gap between the modeled and the observed ENA intensities (and spectral trends) for all six sky regions at energies 50–500 eV. Both ENA models underestimate the observed ENA intensities. At energies below 50 eV, the measured ENA intensities are only upper limits (mind the intervals of uncertainty at the lowest energies) and for the upstream directions, the inflow of neutral ISN H may close the gap. At ENA energies approaching solar wind ion energies in the heliosheath, the observed (IBEX-Lo and IBEX-Hi) and modeled ENA intensities overlap within the measurement uncertainty.

The most notable difference between the two model predictions appears between 30 and 200 eV and is due to the ENAs from heliosheath PUIs (see blue solid and dashed lines in Figure 3). One key difference between the treatment of heliosheath PUIs is that the Boston model assumes a Maxwellian distribution, whereas the Moscow model need not make any assumptions regarding the heliosheath PUIs because of the kinetic treatment. However, the resulting difference in predicted ENA intensities is much smaller than the difference between the models and the observations.

Figure 4 summarizes Figure 2, showing the measured versus modeled ENA energy spectra averaged over all sky regions. The gap, i.e., the discrepancy between modeled and observed ENA intensities that need to be explained, is colored in blue.

5. Discussion

The global underestimation of ENA model predictions versus observations noticed in previous studies (see Section 1) persists for two independent heliosphere models.

This discrepancy is most striking—1 to 2 orders of magnitude in ENA intensity between 50 and 500 eV—where heliosphere models consider only neutralized PUIs to account for observable ENAs. This new study underlines this discrepancy by demonstrating that two independent, sophisticated ENA models result in a similar underestimation. Even more striking is the fact that the gap not only appears toward the nose direction (as already noted by Fuselier et al. 2021) but also toward the heliospheric poles and the downwind hemisphere. This is illustrated in Figure 5, which shows the ratio of modeled over measured ENA intensities for all six sky regions for the Boston (left panel) and for the Moscow model (right panel).

Studying the gap between modeled and measured ENA intensities in all six heliospheric directions, we have considered several options to explain the discrepancy. Some of them are plausible, some of them are unlikely, and some can be ruled out. Here, we rank them from likely to more unlikely. The definite answer to some of these options will have to be the topic of future studies.

1. More intense PUIs in the heliosheath through turbulence: Zirnstein et al. (2021) showed that the IBEX-Hi energy spectrum above 1 keV cannot be reproduced with protons accelerated at the termination shock unless the turbulence power in the termination shock foot and ramp was at least 7 times higher than what was measured by Voyager (e.g., Burlaga et al. 2008). Zirnstein et al. (2018) found that a form of velocity diffusion of 0.15 keV protons in the heliosheath is needed for ENA model fluxes to be consistent with IBEX data from 0.1 to 5 keV. While the authors did not single out the physical process or type of turbulence, they noted that isotropic Kolmogorov turbulence probably was not the main diffusion mechanism. Future studies need to verify if other types of turbulence inside the heliosheath (Opher et al. 2021) or reconnection events could narrow or close the gap between predicted and observed ENA intensities.
2. VLISM sources: If contributions from ENAs within the heliosheath are insufficient, ENA sources in the VLISM must be considered. Possible contributions might come from accelerated ISN hydrogen or from secondary ENAs. The latter would, in contrast to the presumed IBEX Ribbon source, not be organized by the interstellar magnetic field wrapping around the heliopause but more uniformly distributed throughout the VLISM.
3. Possible underestimation of the ISN hydrogen density in heliosphere models: Both models used here assume $n_{H,ISM} = 0.14 \text{ cm}^{-3}$. This density is lower than the $n_{H,ISM} = 0.195 \pm 0.033 \text{ cm}^{-3}$ inferred from PUI measurements (Swaczyna et al. 2020; with $n_H = 0.13 \text{ cm}^{-3}$ at the termination shock). However, it is very unlikely that a change of $n_{H,ISM}$ from 0.14 to 0.195 cm^{-3} could boost the predicted ENA intensities by more than a factor of 2 (also see Kornbleuth et al. 2023a).
4. Interstellar neutrals contribution: ISN O and Ne cannot contribute to the hydrogen signals measured with IBEX-Lo; they are highly constrained in space and energy (Park et al. 2016) and did not contribute to the ENA energy spectra studied in this paper. ISN H and He signals may have contributed to the IBEX-Lo ENA signal as they also produce H^- count rates, but they do so only in the four (ISN He) or two (ISN H) lowest IBEX-Lo energy bins, and only for viewing directions close to the upstream

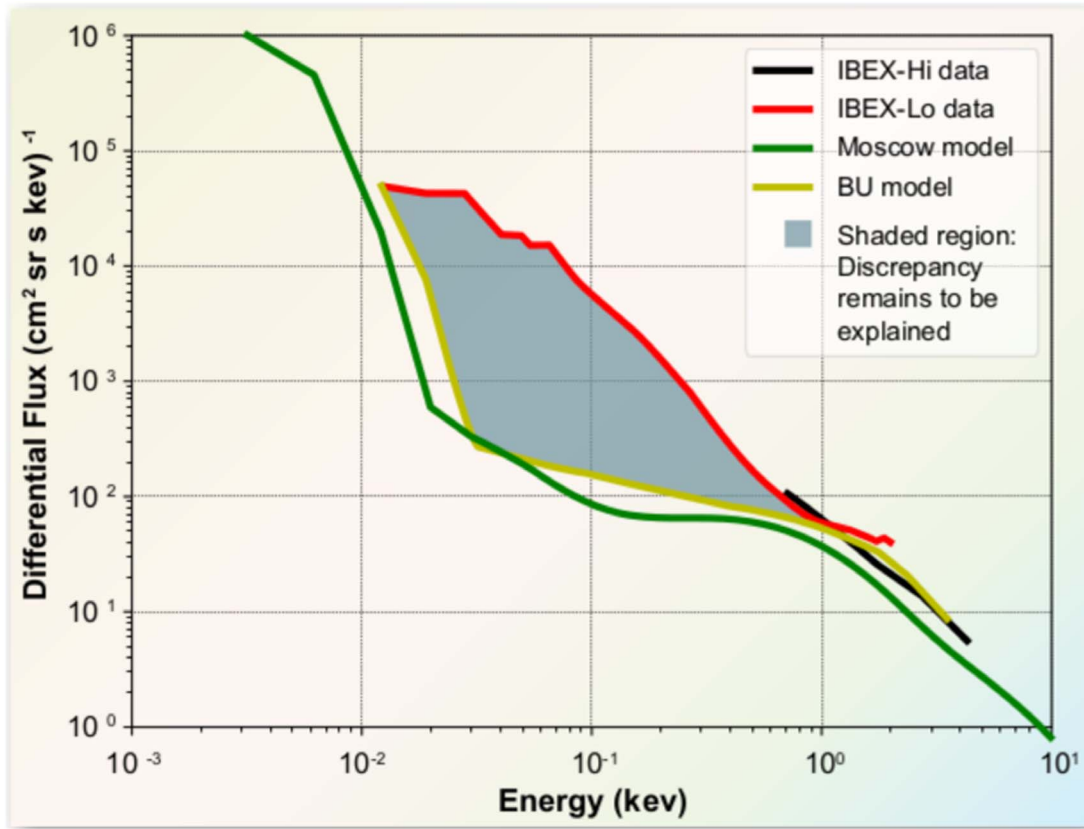


Figure 4. Discrepancy between average measured (red and black lines) and modeled (green lines) ENA intensities.

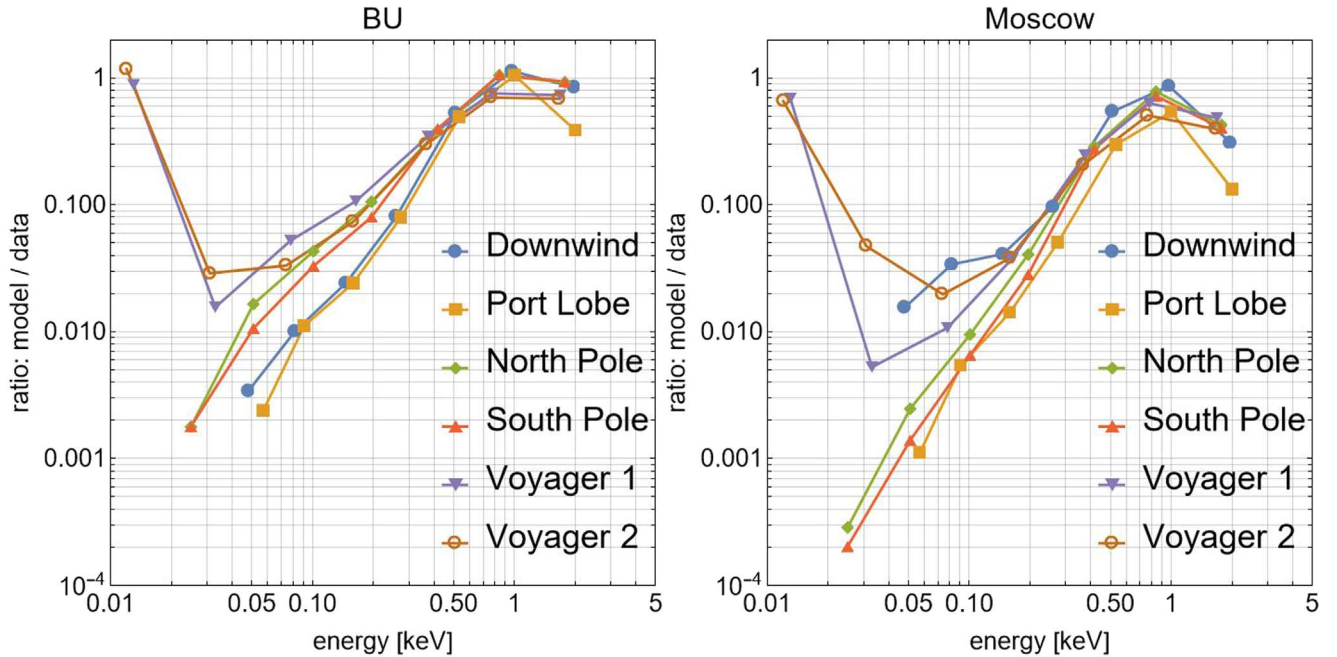


Figure 5. Ratio of modeled over observed ENA intensities for all six sky regions for the Boston University model (left panel) and the Moscow model (right panel).

direction (Galli et al. 2019; Swaczyna et al. 2022). These ISN contributions would explain a part of the discrepancy between the model and observations, but only for the Voyager 1 and Voyager 2 directions (see the model results that take these ISN H contributions into account in

Figures 2 and 3). The inclusion of the secondary ISN He signal in the heliosphere models would partially reduce the gap in these regions around 50 eV. However, ISN contributions cannot account for the gap between 150 and 500 eV for any sky direction.

5. It is unlikely that sufficient numbers of PUIs in the SSW are neutralized inside the termination shock and return to the inner solar system. Normally, PUIs in the SSW do not have a negative velocity component in the solar rest frame before they reach the termination shock. Shocks propagating in the SSW, such as corotating interaction regions, could in principle energize PUIs resulting in ENAs with a net Sunward velocity in the ~ 100 – 200 eV range, but further studies are required to quantify if the predicted ENA signals would reach relevant intensities to explain the observed gap.
6. It is highly unlikely that an additional unidentified local background source in IBEX-Lo data persists constantly over a full solar cycle and accounts for 90% of the total measured signal at 200 eV, whereas it does not contribute anything to ENA countrate at 900 eV.
7. Elevated SW temperature in the heliosheath can be ruled out because of Voyager data (Richardson et al. 2020).
8. The inclusion of neutral helium and helium ions in the heliosphere models would not resolve the 1–2 orders of magnitude discrepancy in hydrogen ENA intensities.

6. Conclusions

Our investigation has highlighted the discrepancy between measured and modeled ENAs from the heliosphere. The gap shows up in all six sky regions studied, for upstream, polar regions, and even for downstream directions. The gap is wide and significant in terms of measurement uncertainties. It is most pronounced at ENA energies around 100 eV. Several options to explain the discrepancy with ENA sources from the heliosheath or beyond are plausible and must be investigated in future studies. In terms of observations, IBEX-Lo will continue to acquire ENA spectra and sky maps over the full energy range from tens of eV up to 2 keV. We are also eagerly awaiting the launch of the IBEX successor Interstellar Mapping and Acceleration Probe (IMAP), scheduled for 2025 (McComas et al. 2018a). Among many other achievements, it will enable the IMAP-Lo instrument to obtain full-sky ENA maps far away from Earth's magnetosphere with improved statistics relative to IBEX-Lo (Sokół et al. 2019b; Schwadron et al. 2022).

Acknowledgments


This study is a part of the Research Team Global Structure of the Heliosphere within the SHIELD NASA DRIVE Science Center. The authors were supported by NASA grant 18-DRIVE18_2-0029, Our Heliospheric Shield, 80NSSC22M0164. J.M.S. and M.A.D. were partially supported by the IBEX mission grant 80NSSC20K0719. K.D. further acknowledges that the work was supported at JHU/APL by NASA under contracts NAS5 97271, NNX07AJ69G, and NNN06AA01C and by subcontract at the Center of Space Research and Technology. M.K., M.O., and M.A.D. also acknowledge support by NASA HGI grant 80NSSC22K0525. I.B. and V.I. acknowledge support from the Russian Science Foundation grant 19-12-00383.

Conflicts of Interest

The authors declare that they have no conflicts of interest.

ORCID iDs

André Galli  <https://orcid.org/0000-0003-2425-3793>
Igor I. Baliukin  <https://orcid.org/0000-0002-8004-0904>

Marc Kornbleuth  <https://orcid.org/0000-0002-3479-1766>
Merav Opher  <https://orcid.org/0000-0002-8767-8273>
Stephen A. Fuselier  <https://orcid.org/0000-0003-4101-7901>
Justyna M. Sokół  <https://orcid.org/0000-0002-4173-3601>
Konstantinos Dialynas  <https://orcid.org/0000-0002-5231-7929>
Maher A. Dayeh  <https://orcid.org/0000-0001-9323-1200>
Vladislav V. Izmodenov  <https://orcid.org/0000-0002-1748-0982>
John D. Richardson  <https://orcid.org/0000-0003-4041-7540>

References

- Alexashov, D. B., Chalov, S. V., Myasnikov, A. V., Izmodenov, V. V., & Kallenbach, R. 2004, *A&A*, **420**, 729
- Baliukin, I. I., Izmodenov, V. V., & Alexashov, D. B. 2020, *MNRAS*, **499**, 441
- Baliukin, I. I., Izmodenov, V. V., & Alexashov, D. B. 2022, *MNRAS*, **509**, 5437
- Baranov, V. B., & Malama, Y. G. 1993, *JGR*, **98**, 15157
- Burlaga, L. F., Ness, N. F., Acuña, M. H., et al. 2008, *Natur*, **454**, 75
- Bzowski, M., Sokół, J. M., Tokumaru, M., et al. 2013, in *Cross-Calibration of Far UV Spectra of Solar System Objects and the Heliosphere*, ISSI Scientific Report Series No.13, ed. E. Quémerais, M. Snow, & R. M. Bonnet (New York: Springer), 67
- Chalov, S. V. 2019, *MNRAS*, **485**, 5207
- Chalov, S. V., Alexashov, D. B., McComas, D., et al. 2010, *ApJL*, **716**, L99
- Dayeh, M. A., Zirnstein, E. J., Desai, M. I., et al. 2019, *ApJ*, **879**, 84
- Decker, R. B., Krimigis, S. M., Roelof, E. C., et al. 2005, *Sci*, **309**, 2020
- Decker, R. B., Krimigis, S. M., Roelof, E. C., et al. 2008, *Natur*, **454**, 67
- Desai, M. I., Allegrini, F. A., Bzowski, M., et al. 2014, *ApJ*, **780**, 98
- Dialynas, K., Galli, A., Dayeh, M. A., et al. 2020, *ApJL*, **905**, L24
- Dialynas, K., Krimigis, S. M., Decker, R. B., et al. 2022, *SSRv*, **218**, 21
- Fraternal, F., Pogorelov, N. V., & Burlaga, L. F. 2020, *ApJL*, **897**, L28
- Funsten, H. O., et al. 2009, *SSRv*, **146**, 75
- Fuselier, S. A., Allegrini, F., Bzowski, M., et al. 2014, *ApJ*, **784**, 89
- Fuselier, S. A., Allegrini, F., Funsten, H. O., et al. 2009a, *Sci*, **326**, 962
- Fuselier, S. A., Bochsler, P., Chornay, D., et al. 2009b, *SSRv*, **146**, 117
- Fuselier, S. A., Galli, A., Richardson, J. D., et al. 2021, *ApJL*, **915**, L26
- Galli, A., Baliukin, I. I., Bzowski, M., et al. 2022a, *SSRv*, **218**, 31
- Galli, A., Wurz, P., Fuselier, S. A., et al. 2014, *ApJ*, **796**, 9
- Galli, A., Wurz, P., Kollmann, P., et al. 2013, *ApJ*, **775**, 24
- Galli, A., Wurz, P., Rahmanifard, F., et al. 2019, *ApJ*, **871**, 52
- Galli, A., Wurz, P., Schwadron, N. A., et al. 2022b, *ApJS*, **261**, 18
- Giacalone, J., Nakanotani, M., Zank, G. P., et al. 2021, *ApJ*, **911**, 27
- Gkioulidou, M., Opher, M., Kornbleuth, M., et al. 2022, *ApJL*, **931**, L21
- Heerikhuisen, J., Pogorelov, N. V., Zank, G. P., et al. 2010, *ApJL*, **708**, L126
- Hsieh, K. C., Giacalone, J., Czechowski, A., et al. 2010, *ApJL*, **718**, L185
- Izmodenov, V., Alexashov, D., & Myasnikov, A. 2005a, *A&A*, **437**, L35
- Izmodenov, V., Malama, Y., & Ruderman, M. S. 2005b, *A&A*, **429**, 1069
- Izmodenov, V., Malama, Y., Gloeckler, G., & Geiss, J. 2004, *A&A*, **414**, L29
- Izmodenov, V., Malama, Y. G., Gloeckler, G., & Geiss, J. 2003, *ApJL*, **594**, L59
- Izmodenov, V. V. 2009, *SSRv*, **143**, 139
- Izmodenov, V. V., & Alexashov, D. B. 2015, *ApJS*, **220**, 32
- Izmodenov, V. V., & Alexashov, D. B. 2020, *A&A*, **633**, L12
- Izmodenov, V. V., & Alexashov, D. B. 2023, *MNRAS*, **521**, 4085
- Izmodenov, V. V., Malama, Y. G., & Ruderman, M. S. 2008, *AdSpR*, **41**, 318
- Katushkina, O. A., Baliukin, I. I., Izmodenov, V. V., & Alexashov, D. B. 2021a, *MNRAS*, **504**, 2501
- Katushkina, O. A., Galli, A., Izmodenov, V. V., & Alexashov, D. B. 2021b, *MNRAS*, **501**, 1633
- Katushkina, O. A., & Izmodenov, V. V. 2010, *AstL*, **36**, 297
- Katushkina, O. A., Izmodenov, V. V., Alexashov, D. B., Schwadron, N. A., & McComas, D. J. 2015, *ApJS*, **220**, 33
- Kleimann, J., Dialynas, K., Fraternal, F., et al. 2022, *SSRv*, **218**, 36
- Kornbleuth, M., Opher, M., Baliukin, I., et al. 2021a, *ApJ*, **921**, 164
- Kornbleuth, M., Opher, M., Baliukin, I., et al. 2021b, *ApJ*, **923**, 179
- Kornbleuth, M., Opher, M., Dialynas, K., et al. 2023b, *ApJL*, **945**, L15
- Kornbleuth, M., Opher, M., Zank, G. P., et al. 2023a, *ApJL*, **944**, L47
- Krimigis, S. M., Mitchell, D. G., Roelof, E. C., Hsieh, K. C., & McComas, D. J. 2009, *Sci*, **326**, 971
- Lallement, R., Quémerais, E., Bertaux, J. L., et al. 2005, *Sci*, **307**, 1447

- Lallement, R., Quémerais, E., Koutroumpa, D., et al. 2010, in AIP Conf. Ser. 1216, Twelfth International Solar Wind Conf., ed. M. Maksimovic et al. (Melville, NY: AIP), 555
- McComas, D. J., Allegrini, F., Bochsler, P., et al. 2009a, *Sci*, 326, 959
- McComas, D. J., Allegrini, F., Bochsler, P., et al. 2009b, *SSRv*, 146, 11
- McComas, D. J., Bzowski, M., Dayeh, M. A., et al. 2020, *ApJS*, 248, 26
- McComas, D. J., Christian, E. R., Schwadron, N. A., et al. 2018a, *SSRv*, 214, 116
- McComas, D. J., Lewis, W. S., & Schwadron, N. A. 2014, *RvGeo*, 52, 118
- McComas, D. J., Zirnstein, E. J., Bzowski, M., et al. 2017, *ApJS*, 229, 41
- Michael, A. T., Opher, M., & Tóth, G. 2018, *ApJ*, 860, 171
- Myasnikov, A. V., Alexashov, D. B., Izmodenov, V. V., & Chalov, S. V. 2000, *JGR*, 105, 5167
- Opher, M., Drake, J. F., Zank, G., et al. 2021, *ApJ*, 922, 181
- Opher, M., Drake, J. F., Zieger, B., et al. 2015, *ApJL*, 800, L28
- Opher, M., Liewer, P. C., Gombosi, T. I., et al. 2003, *ApJL*, 591, L61
- Park, J., Kucharek, H., Möbius, E., et al. 2016, *ApJ*, 833, 130
- Powell, K. G., Roe, P. L., Linde, T. J., Gombosi, T. I., & De Zeeuw, D. L. 1999, *JCoPh*, 154, 284
- Richardson, J. D., Burlaga, L. F., Elliott, H., et al. 2020, *SSRv*, 218, 35
- Schwadron, N. A., Adams, F. C., Christian, E. R., et al. 2014, *Sci*, 343, 988
- Schwadron, N. A., Allegrini, F., Bzowski, M., et al. 2011, *ApJ*, 731, 56
- Schwadron, N. A., Allegrini, F., Bzowski, M., et al. 2018, *ApJS*, 239, 1
- Schwadron, N. A., Möbius, E., McComas, D. J., et al. 2022, *ApJS*, 258, 7
- Sokół, J. M., Kubiak, M. A., Bzowski, M., Möbius, E., & Schwadron, N. A. 2019b, *ApJS*, 245, 28
- Stone, E. C., Cummings, A. C., McDonald, F. B., et al. 2005, *Sci*, 309, 2017
- Stone, E. C., Cummings, A. C., McDonald, F. B., et al. 2008, *Natur*, 454, 71
- Swaczyna, P., Bzowski, M., Christian, E. R., et al. 2016, *ApJ*, 823, 119
- Swaczyna, P., Kubiak, M. A., Bzowski, M., et al. 2022, *ApJS*, 259, 42
- Swaczyna, P., McComas, D. J., Zirnstein, E. J., et al. 2020, *ApJ*, 903, 48
- Tenishev, V., Shou, Y., Borovikov, D., et al. 2021, *JGRA*, 126, e28242
- Tóth, G., Sokolov, I. V., Gombosi, T. I., et al. 2005, *JGRA*, 110, A12226
- Zank, G. P. 2015, *ARA&A*, 53, 449
- Zirnstein, E. J., Heerikhuisen, J., Funsten, H. O., et al. 2016, *ApJL*, 818, L18
- Zirnstein, E. J., Kumar, R., Bandyopadhyay, R., et al. 2021, *ApJL*, 916, L21
- Zirnstein, E. J., Kumar, R., Heerikhuisen, J., McComas, D. J., & Galli, A. 2018, *ApJ*, 860, 170